

Analyzing intensifying thunderstorms over the Congo Basin using the Gálvez-Davison index from 1983–2018

**Kathrin Alber, Ajay Raghavendra,
Liming Zhou, Yan Jiang, Heather
S. Sussman & Stephen L. Solimine**

Climate Dynamics

Observational, Theoretical and
Computational Research on the Climate
System

ISSN 0930-7575

Clim Dyn

DOI 10.1007/s00382-020-05513-x



Your article is protected by copyright and all rights are held exclusively by Springer-Verlag GmbH Germany, part of Springer Nature. This e-offprint is for personal use only and shall not be self-archived in electronic repositories. If you wish to self-archive your article, please use the accepted manuscript version for posting on your own website. You may further deposit the accepted manuscript version in any repository, provided it is only made publicly available 12 months after official publication or later and provided acknowledgement is given to the original source of publication and a link is inserted to the published article on Springer's website. The link must be accompanied by the following text: "The final publication is available at link.springer.com".



Analyzing intensifying thunderstorms over the Congo Basin using the Gálvez-Davison index from 1983–2018

Kathrin Alber¹ · Ajay Raghavendra¹ · Liming Zhou¹ · Yan Jiang¹ · Heather S. Sussman¹ · Stephen L. Solimine¹

Received: 19 May 2020 / Accepted: 19 October 2020
© Springer-Verlag GmbH Germany, part of Springer Nature 2020

Abstract

The Congo Basin situated in equatorial Africa is home to the second largest rainforest on the globe and plays an important role in the Earth's climate system. For instance, the Congo is one of the most convective regions in the world and enhances the tropical large-scale circulation. Although tropical convection is crucial for rainfall and the sustenance of the rainforest, the most intense thunderstorms do not necessarily produce the largest amounts of rainfall over equatorial Africa. Aiming to better understand the decreasing rainfall trend over the Congo, trends in thunderstorm intensity from 1983 to 2018 are analyzed in this paper using the Gálvez-Davison index (GDI), i.e., a thermodynamic index used to measure thunderstorm potential. Consistent with previous studies, thunderstorm activity increased during all seasons over the Congo. The GDI suggests that the increasing trends in thunderstorm activity are attributable to an increase in hydrostatic instability. More specifically, the GDI shows that (1) an increase of cold troughs at 500 hPa, (2) an increase in the temperature gradient between 700 and 950 hPa, and (3) a decrease of the equivalent potential temperature (θ_e) gradient with height collectively act to promote taller, more intense thunderstorms. This study concludes by proposing feedback mechanisms explaining the intensification of thunderstorms. The mechanisms highlight the cooling and moistening of the mid-troposphere, drying and warming at the surface and lower troposphere, and a decrease in vertical stability and convective inhibition. These factors may act to re-enforce the drying trend which has stressed the Congo rainforest over the past 40-years.

Keywords Congo rainforest · Gálvez-Davison index · Rainfall · Thermodynamic stability · Tropical thunderstorms

1 Introduction

Most of the precipitation in the tropics stems from convective rainfall (Dai 2006). Naturally, the majority of the rainfall over the Congo Basin located in equatorial central Africa originates from deep convection and mesoscale convective systems (Jackson et al. 2009). The Congo Basin, Amazonia, and the Indonesian maritime continent form the three most convective regions on the globe and enhance the large-scale tropical circulation (Zipser et al. 2006; Raghavendra et al. 2019). In fact, thunderstorms over the Congo are typically stronger and more intense when compared to other equatorial regions like Amazonia or Indonesia. In spite of its

smaller size, the Congo is characterized by the second largest latent heating rate from convection after the Indonesian maritime continent (Washington et al. 2013). Equatorial Africa is also associated with the greatest annual mean lightning flash rate, having a higher frequency in thunderstorm occurrence and mean flash rate than the rest of the deep tropics (Christian et al. 2003). However, despite the Congo's formidable convection heating rate, thunderstorm intensity and lightning activity, the second largest rainforest in the world, i.e., the Congo Basin, receives less rainfall than Amazonia or Indonesia (Adler et al. 2017). The reduced availability of rainfall exasperates the Congo rainforest's vulnerability to droughts when compared to other major rainforests (Zhou et al. 2014). On a concerning note, trends in the mean rainfall, forest greenness, and dry season length over the Congo Basin indicate a long-term and large-scale drying trend (Zhou et al. 2014; Jiang et al. 2019).

In order to understand rainfall variability and to identify potential drivers for the well-documented decrease in rainfall

✉ Kathrin Alber
kalber2@albany.edu

¹ Department of Atmospheric and Environmental Sciences,
University at Albany, State University of New York, Albany,
NY 12222, USA

over the Congo, there exists a crucial need to understand deep convection. This emphasizes the need to investigate recent trends in thunderstorm activity over the Congo Basin. Despite the decrease in rainfall rates in the Congo Basin, Raghavendra et al. (2018) found an increase in number, size and intensity of thunderstorms over the time period of 1982–2016 during April, May, and June (AMJ), using satellite data. These results were later complemented by other studies which point to a general increase in thunderstorm activity over the Congo Basin throughout the year (e.g., Taylor et al. 2018; Hart et al. 2019; Raghavendra et al. 2019). This seemingly unintuitive relationship between increasing thunderstorm activity and decreasing rainfall over the Congo may be reconciled by Hamada et al. (2015), who demonstrated a weak relationship between thunderstorm intensity and rainfall. However, specific physical mechanisms explaining the complex relationship between tropical deep convection, surface rainfall, and an increase in thunderstorm activity over the Congo have only been incompletely identified. One explanation given for the observed increase in thunderstorm activity over the Congo Basin includes an increase in horizontal wind shear attributed to an increasing temperature contrast between the equator and northern Africa (Taylor et al. 2018).

Thermodynamic stability of the atmosphere is a key ingredient which determines the potential and intensity for atmospheric convection. Often, thermodynamic indices are collectively used to assess the stability of the atmosphere. Although stability indices have been widely used to forecast thunderstorms (e.g., Haklander and Van Delden 2003; Jayakrishnan and Babu 2014), Gálvez and Davison (2016) found that traditional stability indices often lack skill when attempting to predict tropical convection since the processes driving convection differ between the tropics and the extra tropics, and stability plays a different role in the development of moist convection. Quantifying tropical convection can be challenging since the skill of traditional stability indices like the Lifted-Index (LI), K-Index (KI), Showalter-Index (SI) or convective available potential energy (CAPE) in predicting deep convection is limited for the tropics (Uma and Das 2019).

In the mid-latitudes, convection can be triggered by dynamic processes (e.g., frontal systems). However, tropical convection depends more on column stability and thermodynamic processes since dynamical processes are usually weak. Aiming to improve forecasts for tropical convection, the Gálvez-Davison Index (GDI) was developed by the NOAA Weather Prediction Center (WPC) in 2014, focusing on thermodynamic processes more than on dynamical processes (Gálvez and Davison 2016). Miller et al. (2019) utilized the GDI and other stability indices to forecast rainfall in Puerto Rico and found that CAPE, the KI and Total Totals had very little skill when compared to

the GDI. Since the GDI is a relatively new index, follow-up studies are limited in numbers. In this study, the GDI and its sub-indices are utilized to investigate the increasing trends in thunderstorm activity over the Congo during different seasons, and thus providing a perspective to understand thermodynamic characteristics of thunderstorm as well as profound indications of changes in thunderstorm activity. The physical processes influencing the GDI trends are later diagnosed in order to gain a better understanding about the increasing trend in a thunderstorm activity and decreasing trend in rainfall over the Congo.

2 Data

This study focuses on the Congo Basin, which is defined as the area from 5° N–5° S and 12° E–25° E. All four seasons, i.e., December, January, February (DJF), March, April, May (MAM), June, July, August (JJA) and September, October, November (SON) were examined. MAM and SON are the two wet seasons and DJF and JJA are the two dry seasons (Pokam et al. 2012; Dyer et al. 2017), where dry seasons in the tropics represent yearly periods with low amounts of rainfall, which coincide with the seasonal shift of the tropical rain belt (Nicholson 2018; Jiang et al. 2019). Two different datasets were used in this study, i.e., a satellite and reanalysis dataset.

2.1 GridSat-B1 satellite data

Infrared (IR) channel brightness temperature (T_b) from the Gridded Satellite (GridSat-B1) dataset sampled by the European Meteosat (MET) series of geostationary satellites, available from 1981–present (Knapp 2008; Knapp et al. 2011), was used in this study. The GridSat-B1 dataset was created by remapping and merging the International Satellite Cloud Climatology Project (ISCCP) B1 data onto $0.07^\circ \times 0.07^\circ$ grids using nearest-neighbor sampling at a 3-h temporal resolution. The GridSat-B1 dataset provides a uniform set of quality controlled geostationary satellite observations for the visible ($0.7 \mu\text{m}$), infrared window ($11.0 \mu\text{m}$) and infrared water vapor ($7.7 \mu\text{m}$) channels. However, only the IR channel T_b has received more extensive inter-satellite calibration and is thus identified as a Climate Data Record (NRC 2004). Raghavendra et al. (2020b) reported large volumes of missing data between 1982 and 1985 in the GridSat-B1 data record. However, T_b from 1983 to 2018 was used in this study since seasonal means were used, and missing data is occurring in smaller chunks.

2.2 ERA-Interim reanalysis data

The ERA-Interim dataset (ERA-I; Dee et al. 2011) was used to obtain atmospheric temperature and specific humidity at 950 hPa, 850 hPa, 700 hPa and 500 hPa, and zonal (u) and meridional (v) wind at 850 hPa and 500 hPa at a $0.7^\circ \times 0.7^\circ$ spatial resolution. Although reanalysis products other than the ERA-I dataset could have been utilized for this study, the lack of surface observations and radiosonde networks over the Congo Basin makes it challenging to identify the most accurate reanalysis dataset (Washington et al. 2013; Hua et al. 2019). However, the bias and the root-mean-square error associated with the ERA-I wind field is found to be comparable to other reanalysis datasets and therefore the ERA-I dataset is found to be adequate for this study (Hua et al. 2019).

The ERA-I dataset was produced by the European Centre for Medium-Range Weather Forecasts (ECMWF) using the Integrated Forecast System (IFS) release Cy31r2 which was used for operational forecasting between 12 December 2006 and 5 June 2007 (Dee et al. 2011). Since the GDI was developed for the operational analysis and forecasting of tropical convection, the atmosphere needs to be evaluated before convection has occurred. Over the Congo Basin, thunderstorm activity is strongly influenced by the tropical diurnal cycle (Yang and Slingo 2001) and convection usually peaks between 15:00 and 18:00 UTC. Therefore, monthly mean data at 12:00 UTC was used from the ERA-I reanalysis dataset for all calculations to evaluate thunderstorm activity at 15:00 UTC using satellite observations from the GridSat-B1 data. The ECMWF forecast model is regarded as one of the most accurate numerical weather prediction model in the meteorological model community (Buizza et al. 2005; Wedam et al. 2009; Perez et al. 2010), therefore the ERA-I reanalysis dataset is also likely to be the best reanalysis dataset choice for this study due to the 3-h lag in evaluating the reanalysis data (atmospheric variables) and satellite observations (thunderstorm activity).

2.3 Dataset limitations

The GridSat-B1 dataset was derived from more than 30 geostationary satellites (Knapp 2008) and the data covering the Congo Basin was sampled by the European Meteosat (MET) series of geostationary satellites (MET 2–10) that provide excellent coverage over Central Africa (Raghavendra et al. 2018). Despite improved data processing and inter-satellite calibrations (Knapp 2012), the possibility that long-term trends estimated from the GridSat-B1 may suffer from biases associated with inter-satellite calibrations, satellite view zenith effects, gaps in coverage, and differences in instrument spectral response functions cannot be excluded

(Knapp 2016). Therefore, higher-quality datasets and modeling work will be included in future studies.

Differences and uncertainties among different reanalysis products, climate model simulations and satellite derived datasets over the Congo Basin (Diem et al. 2014; Hua et al. 2019), and the lack of observations to validate the model outputs and reanalysis data (Washington et al. 2013; Alsdorf et al. 2016) represent a major challenge for scientific studies over the Congo. A limitation of this study therefore includes the poor correlation between different observation and reanalysis datasets over the Congo Basin, especially for moisture fields (Lee and Biasutti 2014). The fact that only one reanalysis dataset was used represents another limitation of this study. But, the data requirements for the analysis performed for this study are very specific, i.e., daily data at 12:00 UTC for specific pressure levels at a fine resolution. Therefore, only one reanalysis dataset was analyzed.

3 Methods

3.1 Thunderstorm detection

In order to evaluate thunderstorm activity and trends using satellite data, low T_b values (e.g., $T_b < -50^\circ\text{C}$) were used to detect cold cloud top temperatures, which may be used to quantify thunderstorm spatial extent and intensity. The lower the T_b , the deeper the convection and the stronger the intensity of the storm (Raghavendra et al. 2018). In order to detect intense thunderstorms over the Congo, cold cloud fraction with T_b between -50 and -70°C was estimated from the re-gridded GridSat-B1 data by calculating the percentage (%) of pixels with T_b between -50 and -70°C within each $0.98^\circ \times 0.98^\circ$ grid.

3.2 The Galvez-Davison index (GDI) its sub-indices

The GDI was calculated as a measure of thunderstorm potential over the Congo Basin. It consists of three different sub-indices analyzing different physical processes and a terrain correction, and is calculated as follows:

$$GDI = CBI + MWI + II + TC \quad (1)$$

where the three sub-indices are the Column Buoyancy Index (CBI) considering the availability of heat and moisture in the middle and lower troposphere, the Mid-Tropospheric Warming Index (MWI) considering stabilizing and destabilizing effects of mid-level ridges and troughs, and the Inversion Index (II) considering entrainment of dry air and stabilization associated with trade wind inversions. There is also an optional terrain correction (TC) that can be added. GDI values range from around -20 to $+45$, indicating the thunderstorm potential. GDI values of -20 indicate fair conditions

and shallow convection producing very light, isolated rain. GDI values around +45 indicate a high potential for scattered to widespread thunderstorms.

In order to calculate the GDI and its sub-indices, temperature and specific humidity at four vertical levels, i.e., 950 hPa, 850 hPa, 700 hPa, and 500 hPa were obtained from the ERA-I data. Those four vertical levels are used to define three layers, i.e., A, B, and C. A evaluates the conditions at 950 hPa, B evaluates the conditions averaged over 850 hPa and 700 hPa, and C evaluates the conditions at 500 hPa (Gálvez and Davison 2016). Specific humidity and temperature data was used in order to obtain relative humidity for each level (Bolton 1980; Brock and Richardson 2001). The formulas used to derive mixing ratios (r), potential temperature (θ), and equivalent potential temperature (θ_e) proxies for each layer (Betts and Dugan 1973; Bolton 1980; Gálvez and Davison 2016), which are needed to calculate the GDI, are documented in Appendix A.

3.3 Column buoyancy index (CBI)

The CBI analyzes moisture availability and temperature of the layers A and C by calculating the θ_e of those layers. The CBI is an enhancement factor and produces positive values. It is the only sub-index of the GDI producing positive values. The higher the CBI is, the larger is the potential for deep convection. Deep convection is characterized by a warm and moist mid tropospheric layer (ME) which is being reinforced by a warm and moist layer in the lower troposphere (LE). A high CBI therefore indicates the presence of a deep moist layer, leading to deep convection and potential heavy rainfall. The CBI is calculated as follows:

$$ME = \theta_{e(C)} - \beta \tag{2}$$

$$LE = \theta_{e(A)} - \beta \tag{3}$$

$$CBI = \begin{cases} \gamma \times LE \times ME, & LE > 0 \\ 0, & LE \leq 0 \end{cases} \tag{4}$$

where $\beta = 303$ K is an empirical constant, which is used to set a lower boundary for the availability of heat and moisture in the boundary layer, and $\gamma = 6.5 \times 10^{-2} \text{ K}^{-1}$ is an empirical scaling factor used to obtain values comparable to the relatively better-known K-Index (Gálvez and Davison 2016).

3.4 Mid tropospheric warming/stabilization index (MWI)

By calculating the temperature of layer C, the MWI considers mid tropospheric stabilization induced by warm ridges and destabilization by cold troughs. The MWI is an

inhibition factor producing negative values. If temperatures are higher than the threshold $\tau = 263.15$ K, MWI values are negative, indicating strong inhibition of convection and stabilization of the layer by a warm ridge. The MWI is calculated as follows:

$$MWI = \begin{cases} \mu \times (T_{500} - \tau), & T_{500} - \tau > 0 \\ 0, & T_{500} - \tau \leq 0 \end{cases} \tag{5}$$

where $\mu = -7 \text{ K}^{-1}$ is an empirical scaling factor which introduces a negative sign, and controls the relative weight of the MWI in the GDI formula (Gálvez and Davison 2016).

3.5 Inversion index (II)

The II aims to include the effects of trade wind inversions. Like the MWI, the II is an inhibition factor, producing negative values. The II considers the stabilizing effects of inversions and dry air entrainment, which act to inhibit convection. A stability factor (II_S) is calculated by taking the difference in temperature between 950 and 700 hPa, with lower values of II_S indicating stronger stabilization. To take dry air entrainment into account, the difference in θ_e between the layers A and B is considered, and a drying factor (II_D) is calculated. The lower and more negative II_D , the larger the decrease of θ_e with height, indicating the occurrence of dry air and subsidence, leading to inhibition of convection. A low II_S and II_D leads to a low value for II and represents an inhibition of convection and vice-versa. The II is calculated as follows:

$$II_S = T_{950} - T_{700} \tag{6}$$

$$II_D = \theta_{e(B)} - \theta_{e(A)} \tag{7}$$

$$II = \begin{cases} 0, & II_S + II_D > 0 \\ \sigma \times (II_S + II_D), & II_S + II_D \leq 0 \end{cases} \tag{8}$$

where $\sigma = 1.5 \text{ K}^{-1}$ is an empirical factor to control the weight of the II in the GDI formula (Gálvez and Davison 2016).

3.6 Terrain correction (TC)

To improve visualization over higher terrain, a TC factor can be added, which may be calculated as follows:

$$TC = P_3 - \frac{P_2}{P_{SFC} - P_1} \tag{9}$$

where $P_1 = 500$ hPa, $P_2 = 9000$ hPa, $P_3 = 18$ hPa which are empirical constants, and P_{SFC} is the surface pressure (hPa) (Gálvez and Davison 2016). The TC was not included in the GDI calculation in this study since the study region

only experienced relatively small spatial variations in topography from 12 to 25° E (e.g., Raghavendra et al. 2020a). Furthermore, the mean surface pressure within the Congo Basin is ~960 hPa which results in a relatively small value of TC \cong 1.5, and dynamic fields such as surface pressure show relatively little variability in the tropics especially for seasonal timescales. Therefore, neglecting the TC term has an insignificant impact on the results presented in this paper. To clarify, the TC term should be included if the analysis or forecast period is under two weeks especially at higher elevations.

3.7 Wind shear

Since the Coriolis parameter and the horizontal temperature gradient are very small near the equator, dynamic–thermodynamic indices such as the Eady growth rate (e.g., Raghavendra and Milrad 2019) are of little use. However, dynamics such as wind shear should not be ignored when diagnosing thunderstorms since vertical wind shear influences the structure and organization of convective systems, as well as their evolution (Marion and Trapp 2019; Raghavendra et al. 2020a). Vertical wind shear can organize convection into convective clusters and squall lines producing intense precipitation and extending the lifetime of convective systems (Robe and Emanuel 2001; Anber et al. 2014). Wind shear also advects moisture and temperature which impact thermodynamic stability (Robe and Emanuel 2001). Therefore, a relatively simple approach was used to calculate and analyze the vertical wind shear, i.e., $\text{Wind shear} = \left| \frac{\vec{V}}{500} \right| - \left| \frac{\vec{V}}{850} \right|$.

3.8 Trend analysis

To quantify long-term changes of thunderstorm activity over the Congo, seasonal trends and interannual variability of cold cloud fraction, the GDI and its sub-indices, and wind shear were calculated. The linear trend was estimated based on least square regression at both the grid and regional levels. The statistical significance (p-value) of the linear regression was evaluated using the two-tailed Student's test.

4 Results

4.1 More vigorous thunderstorms diagnosed by cold cloud top temperatures

In order to quantify changes in thunderstorm activity using satellite data, the cold cloud fraction (%) with T_b ranging between -50 and -70 °C was calculated. This served as a method to quantify intense thunderstorms over the Congo, as intense storms are characterized by $T_b < -50$ °C.

Figure 1a–d shows spatial patterns of the seasonal climatology and trends in cold cloud fraction, indicating an increase in cold cloud fraction over large parts of the study region for all seasons. The seasonal cycle can also be observed in Fig. 1a–d. The north- and southward movement of the tropical rain belt is visible, as the tropical rain belt is characterized by enhanced convection and therefore higher percentages of cold cloud fraction. The green contours show the climatological values of the cold cloud fraction (%). The highest values, representing the tropical rain belt, are located south of the equator in DJF, and then shift northwards to the equator in MAM. In JJA, the highest values lie north of the equator in JJA, and then shift back south again during SON (Nicholson 2018).

Figure 1e shows the interannual variability of the cold cloud fraction averaged over the study region and indicates significant increases in cold cloud fraction of 0.03–0.04% year⁻¹ ($p < 0.10$) during all months. The detected increases in cold cloud fraction suggests that the spatial extent of thunderstorms over the Congo has been increasing during all seasons. This is consistent with previous works such as Hart et al. (2019) and Raghavendra et al. (2018) showing a widespread increase in the areal extent and intensity of thunderstorms over the Congo over the past 30 years, and Chou and Chen (2010) showing an increase in convection depth in a warmer climate.

4.2 Changes in GDI and its sub-indices

Seasonal trends in GDI show a significant increase over large parts of the Congo (Fig. 2a–d), with the GDI significantly increasing during all seasons (0.1–0.17 year⁻¹; $p < 0.10$). The largest increase of 0.17 year⁻¹ is detected in MAM and JJA, followed by SON with an increase of 0.12 year⁻¹, and DJF with the lowest increase of 0.1 year⁻¹ (Fig. 2e). This increase in GDI suggests a significant increase in thunderstorm activity over the Congo during all seasons, which is consistent with the trends detected in cold cloud fraction. Aiming to discover the physical mechanisms responsible for the increase in thunderstorm activity, the different sub-indices of the GDI were analyzed separately. First, the observed trends in the GDI sub-indices are presented, and later complemented by an explanation for each trend detected in the GDI.

The CBI shows a small but insignificant decrease over most of the Congo during all seasons (Fig. 3a–e). This leads to the conclusion that the interannual variability of the CBI does not contribute to the increase in thunderstorm activity. In contrast to that, the MWI is becoming weaker over most parts of the Congo, with the strongest and most significant trend in JJA, followed by MAM and SON, with DJF exhibiting the weakest trend (Fig. 4a–d). The interannual variability indicates a trend of 0.10 year⁻¹ ($p < 0.10$).

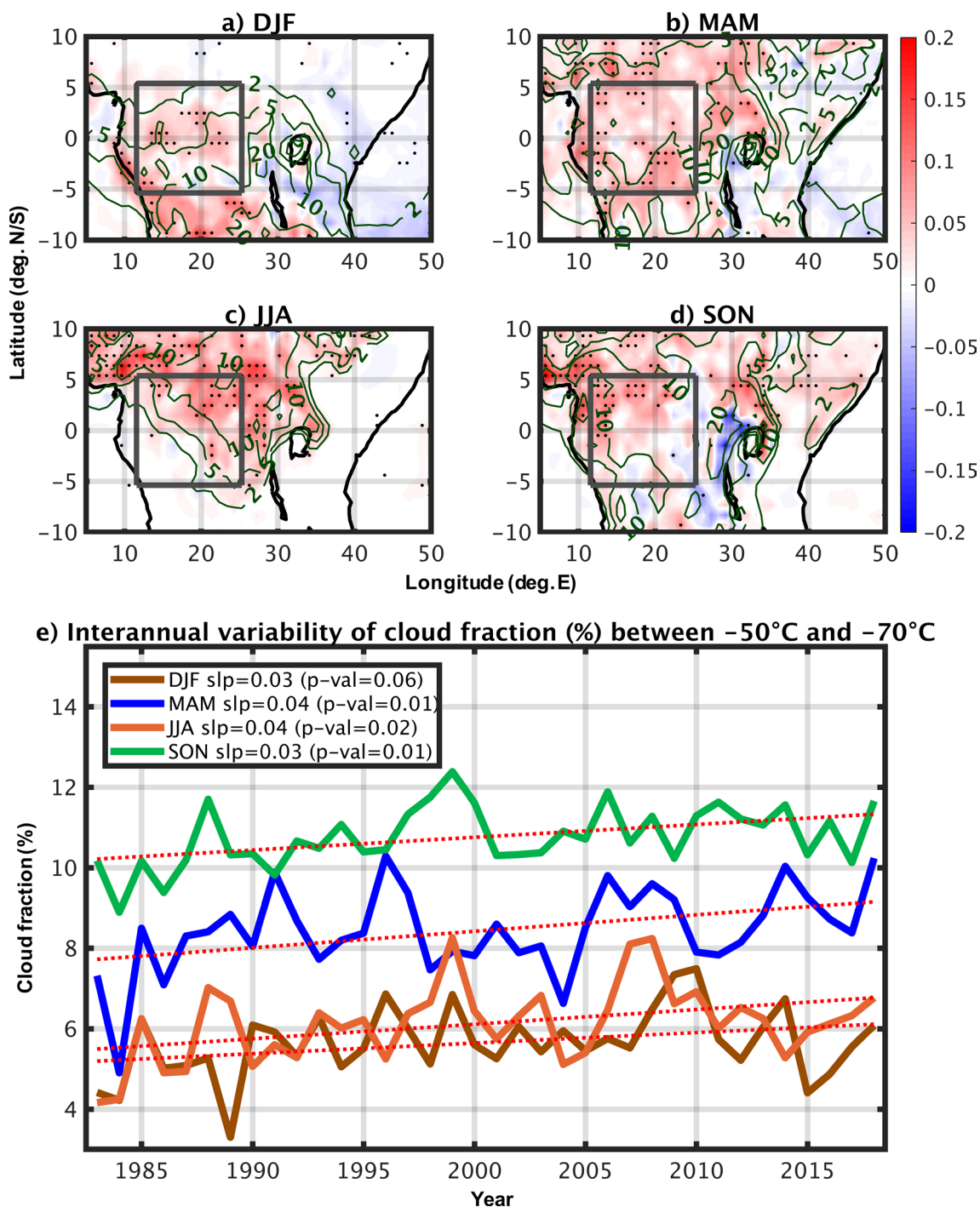


Fig. 1 a–d Seasonal trends in cloud fraction ($\% \text{ year}^{-1}$) for T_b between -50 and -70 °C at 15:00 UTC from 1983 to 2018. Gray boxes (5° N – 5° S and 12° E – 25° E) represent the Congo Basin. Trends significant at $p < 0.05$ are shown using a black dot. The green

lines show the climatological values of the cloud fraction (%) from 1983 to 2018. **e** Interannual variability and trends of the seasonal mean cloud fraction with T_b ranging from -50 to -70 °C at 15:00 UTC from 1983 to 2018 over the Congo Basin

in JJA, 0.09 year^{-1} ($p < 0.10$) in MAM and 0.05 year^{-1} ($p < 0.10$) in SON. The trend for DJF is not significant at

$p < 0.10$ (Fig. 4e). Thus, the MWI likely contributes to the increasing thunderstorm activity in MAM, JJA and SON.

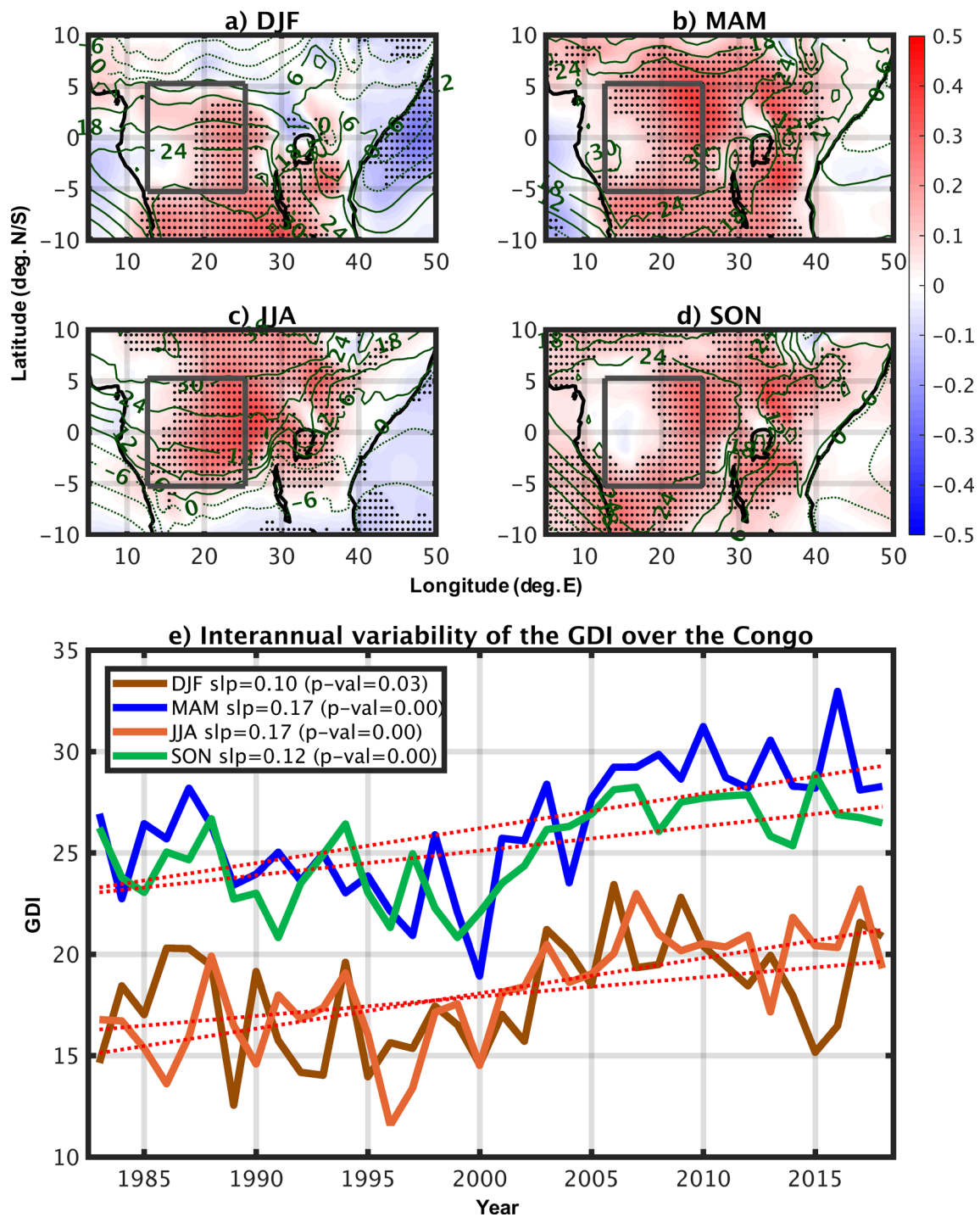


Fig. 2 a–d Seasonal trends in GDI (GDI year⁻¹) at 12:00 UTC from 1983 to 2018. Gray boxes (5° N–5° S and 12° E–25° E) represent the Congo Basin. Trends significant at $p < 0.05$ are shown using a black

dot. The green lines show the climatological values of the GDI from 1983 to 2018. e Interannual variability of the GDI at 12:00 UTC from 1983 to 2018 over the Congo Basin

The II is also becoming weaker during all seasons with significant trends in almost the entire study region (Fig. 5a–d). The interannual variability shows trends of 0.10–0.11 year⁻¹ ($p < 0.10$) during all seasons (Fig. 5e).

Since the II is the sum of two terms i.e., II_D and II_S , these terms were also analyzed separately. The II_D became weaker over the entire study region (Fig. 6a–d), and the linear trend in the II_D increased by 0.07–0.08 year⁻¹

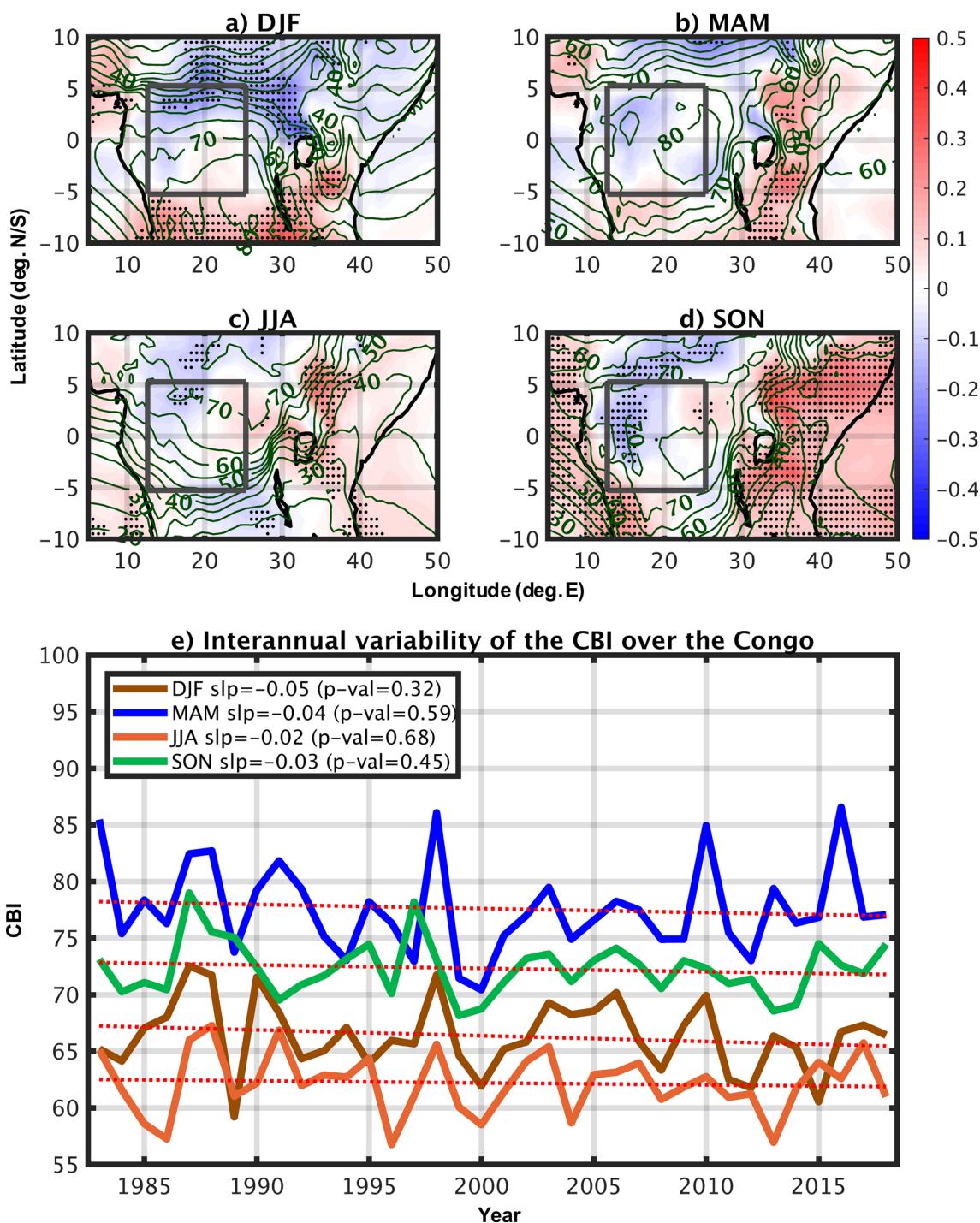


Fig. 3 a–d Seasonal trends in CBI (CBI year⁻¹) at 12:00 UTC from 1983 to 2018. Gray boxes (5° N–5° S and 12° E–25° E) represent the Congo Basin. Trends significant at $p < 0.05$ are shown using a black

dot. The green lines show the climatological values of the CBI from 1983 to 2018. e Interannual variability of the CBI at 12:00 UTC from 1983 to 2018 over the Congo Basin

($p < 0.10$) during all seasons as well (Fig. 6e). A smaller Π_D suggests that the θ_e gradient is decreasing with height and the entrainment of dry air over the inversion

is becoming less frequent. This ultimately results in enhanced convection and thunderstorm activity (James and Markowski 2010). The Π_S shows an increasing trend over most of the Congo Basin, and the interannual variability

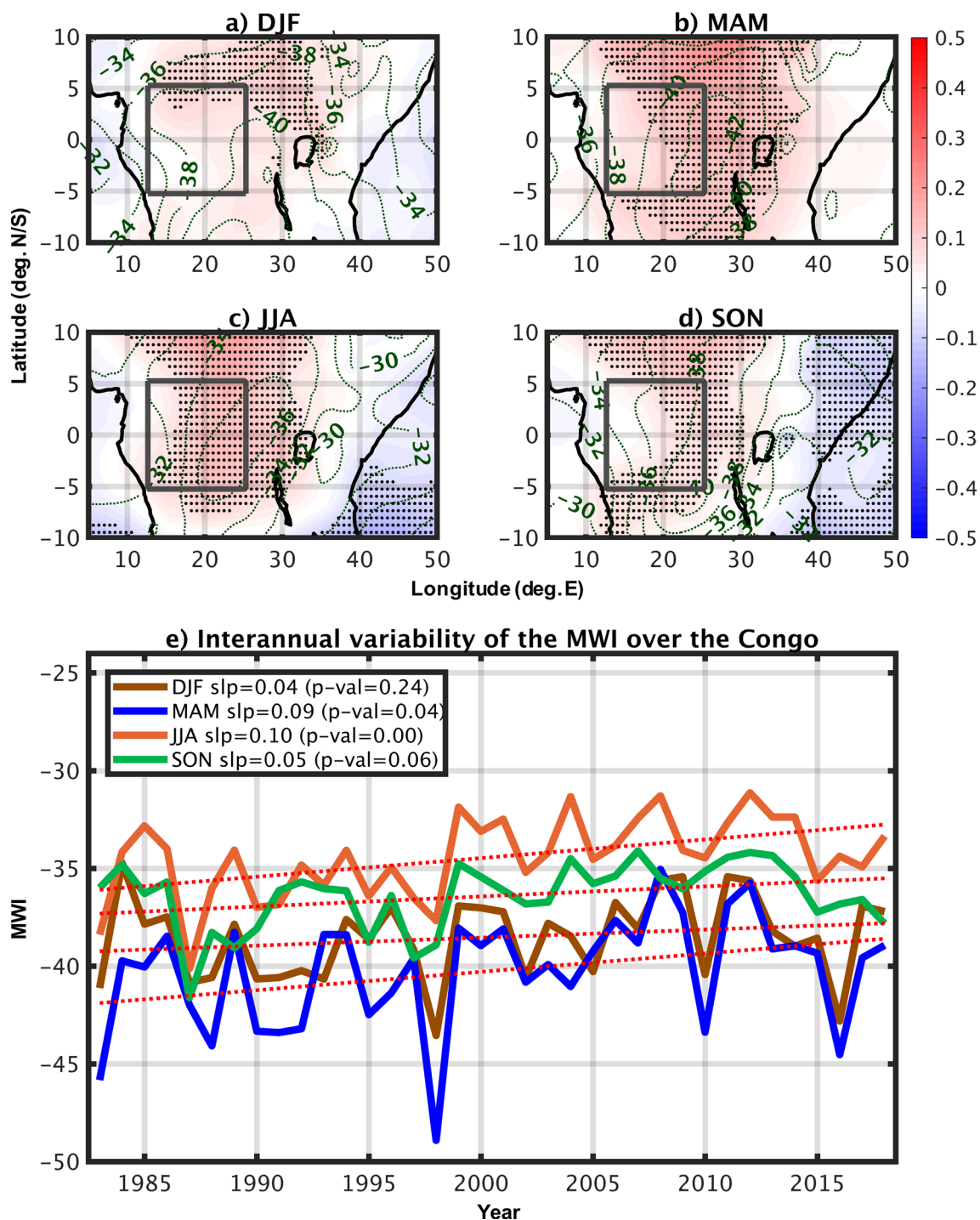


Fig. 4 a–d Seasonal trends in MWI (MWI year⁻¹) at 12:00 UTC from 1983 to 2018. Gray boxes (5° N–5° S and 12° E–25° E) represent the Congo Basin. Trends significant at $p < 0.05$ are shown using a black

dot. The green lines show the climatological values of the MWI from 1983 to 2018. **e** Interannual variability of the MWI at 12:00 UTC from 1983 to 2018 over the Congo Basin

increased by 0.03–0.07 year⁻¹ (Fig. 7) depending on the season, with DJF exhibiting the largest increase, followed by MAM, JJA and SON. These findings indicate that the temperature gradient between 950 and 700 hPa

is increasing, leading to a decrease in stability of the column and therefore supporting an increase in tropical convection.

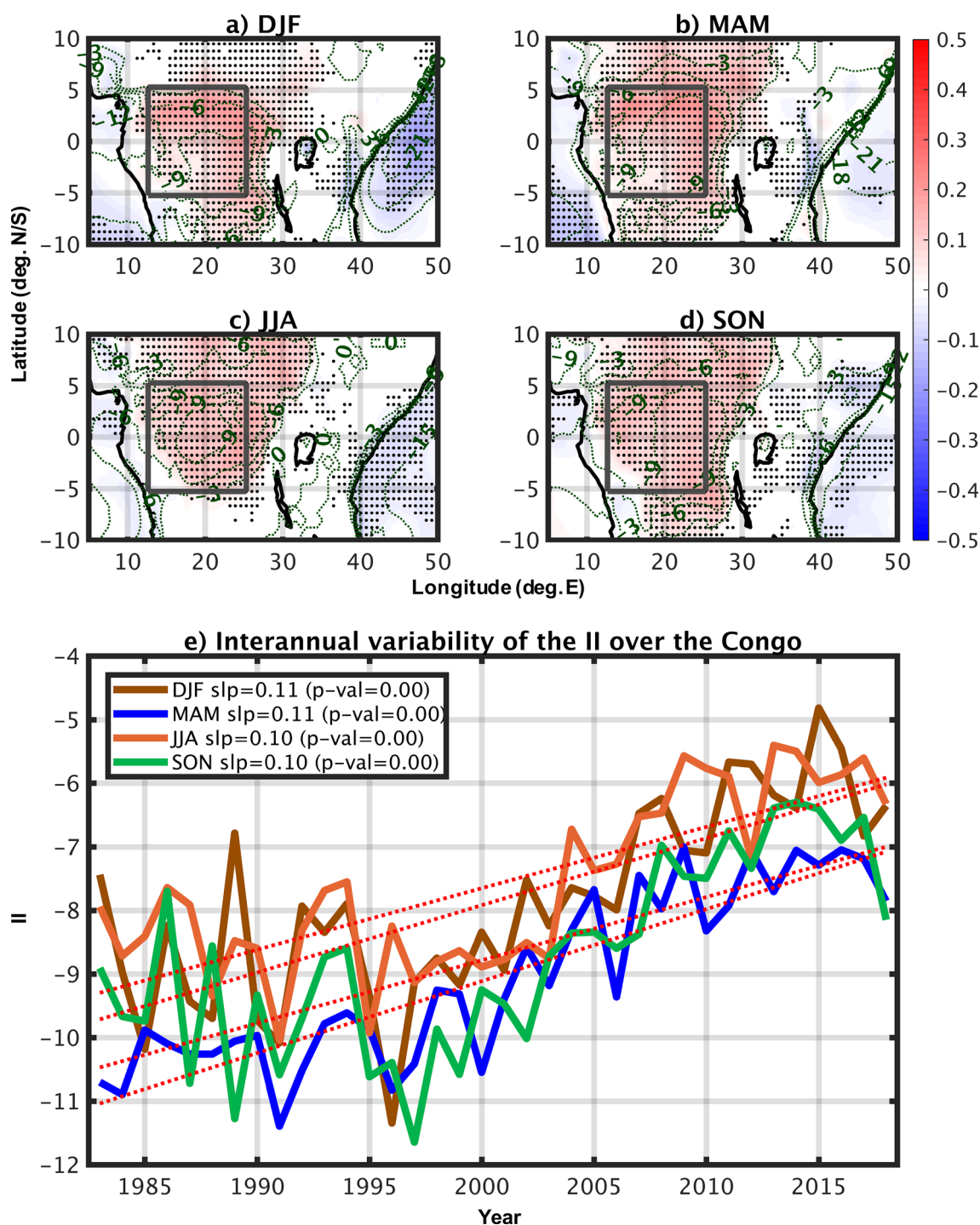


Fig. 5 a–d Seasonal trends in II (II year⁻¹) at 12:00 UTC from 1983 to 2018. Gray boxes (5° N–5° S and 12° E–25° E) represent the Congo Basin. Trends significant at $p < 0.05$ are shown using a black

dot. The green lines show the climatological values of the II from 1983 to 2018. **e** Interannual variability of the II at 12:00 UTC from 1983 to 2018 over the Congo Basin

4.3 Wind shear

Wind shear was found to be increasing significantly over the Congo during all seasons besides DJF. An increase of

0.03–0.07 ms⁻¹ year⁻¹ ($p < 0.10$) is shown with the largest increase in SON, followed by JJA and MAM (Fig. 8). This presents an additional factor potentially contributing to the increase in thunderstorm activity since wind

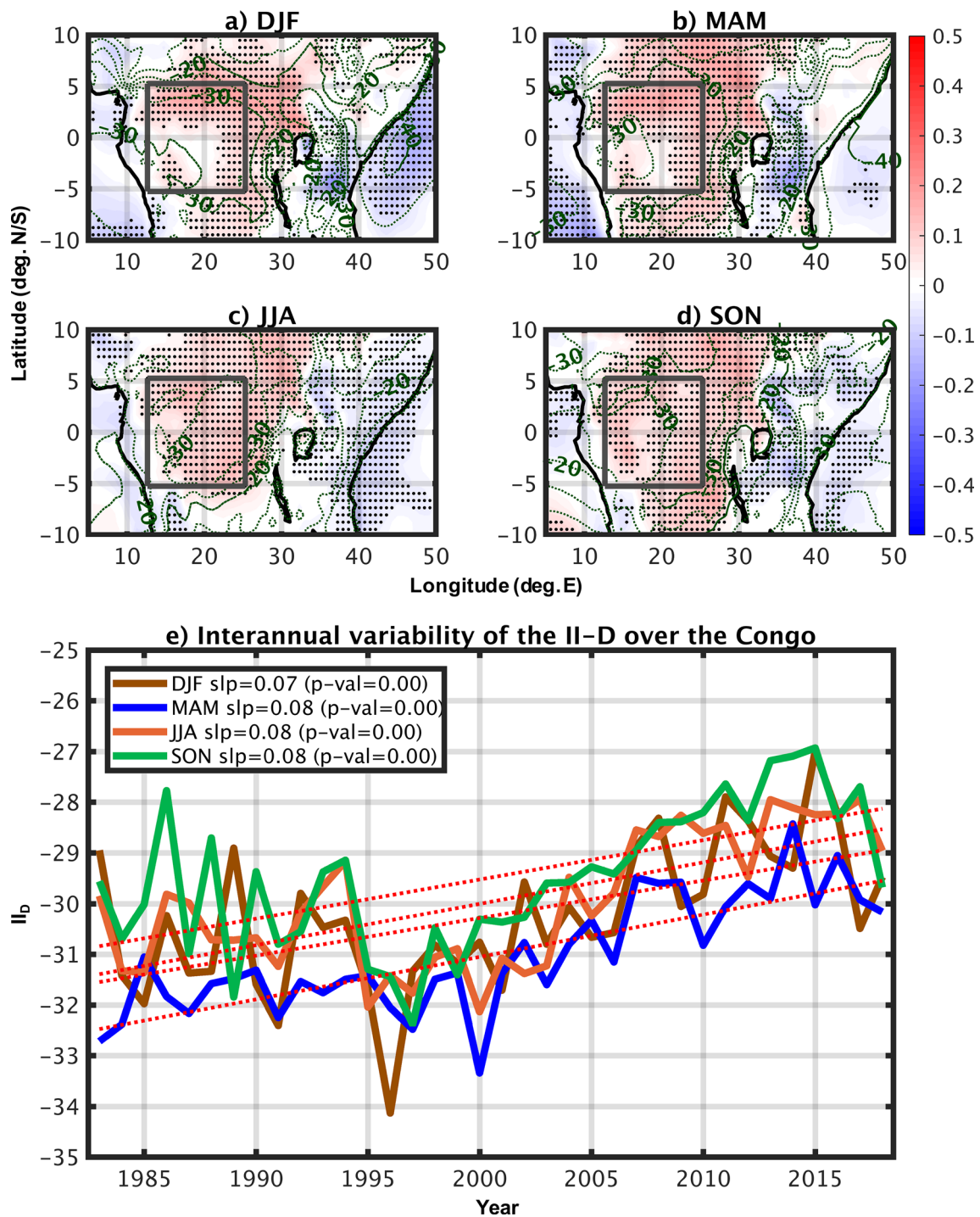


Fig. 6 a–d Seasonal trends in II_D ($\text{II}_D \text{ year}^{-1}$) at 12:00 UTC from 1983 to 2018. Gray boxes ($5^\circ \text{ N}–5^\circ \text{ S}$ and $12^\circ \text{ E}–25^\circ \text{ E}$) represent the Congo Basin. Trends significant at $p < 0.05$ are shown using a black

dot. The green lines show the climatological values of the II_D from 1983 to 2018. **e** Interannual variability of the II_D at 12:00 UTC from 1983 to 2018 over the Congo Basin

shear and orography significantly influence convection and precipitation over the Congo Basin. The unique African orography with the East African highlands and the Ethiopian highlands located in the northeast of the Congo modifies wind patterns by blocking tropical easterlies

(zonal wind) and intensifying meridional wind around the mountain. This increase in wind shear potentially results in well-organized and intense thunderstorms over the Congo Basin (Marion and Trapp 2019; Raghavendra et al. 2020a).

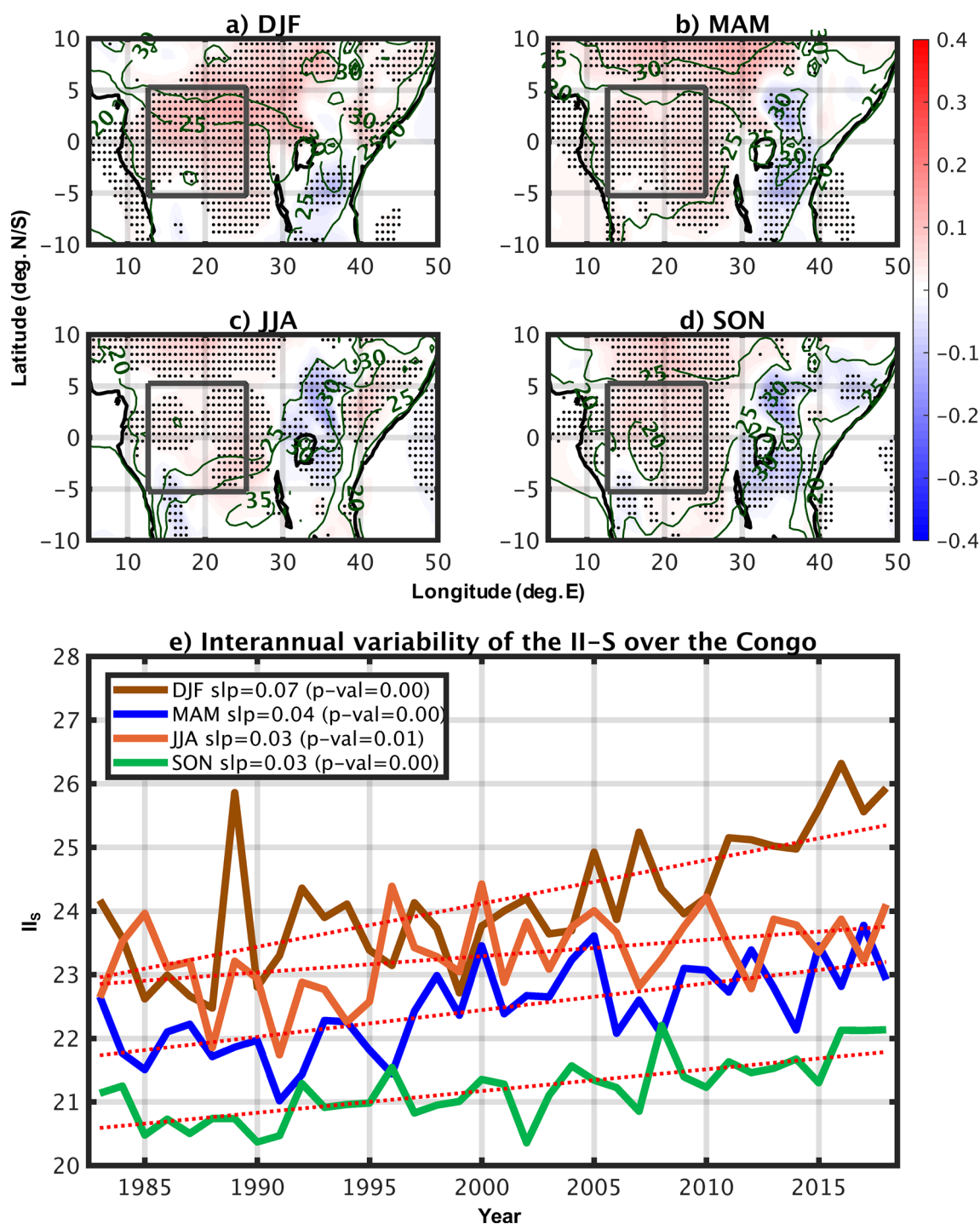


Fig. 7 a–d Seasonal trends in II_S ($II_S \text{ year}^{-1}$) at 12:00 UTC from 1983 to 2018. Gray boxes ($5^\circ \text{ N}–5^\circ \text{ S}$ and $12^\circ \text{ E}–25^\circ \text{ E}$) represent the Congo Basin. Trends significant at $p < 0.05$ are shown using a black

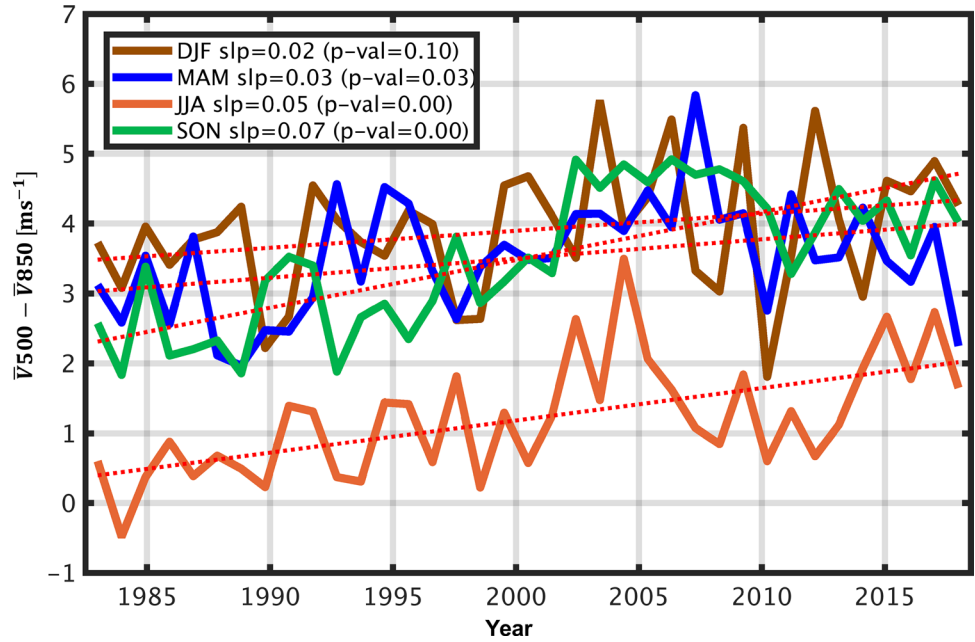
dot. The green lines show the climatological values of the II_S from 1983 to 2018. **e** Interannual variability of the II_S at 12:00 UTC from 1983 to 2018 over the Congo Basin

5 Discussion and conclusion

In this study, thunderstorm activity over the Congo is analyzed using satellite-derived cold cloud top temperatures

and the GDI including its sub-indices (CBI, MWI, and II). The GDI is a thermodynamic index developed to better diagnose tropical convection, with the CBI analyzing the availability of heat and moisture in the middle and lower troposphere, the MWI considering stabilizing and

Fig. 8 Interannual variability in wind shear between 500 and 850 hPa ($\text{ms}^{-1} \text{year}^{-1}$) at 12:00 UTC from 1983 to 2018 over the Congo Basin



destabilizing effects of mid-level ridges and troughs, and the II considering entrainment of dry air and stabilization associated with trade wind inversions. The results show an increasing trend in convective activity over the Congo during all seasons from 1983 to 2018, which is consistent with previous findings indicating an increase in the extent and intensity of thunderstorms over equatorial

Africa (e.g., Raghavendra et al. 2018; Taylor et al. 2018; Hart et al. 2019). The increase in thunderstorm activity is found to be the result of three processes: (1) a cooling of the 500 hPa temperature, which may be attributable to an increase in cold troughs, diagnosed using the MWI, (2) an increase in the temperature gradient between 700 and 950 hPa, diagnosed using the II_S , and (3) a decrease

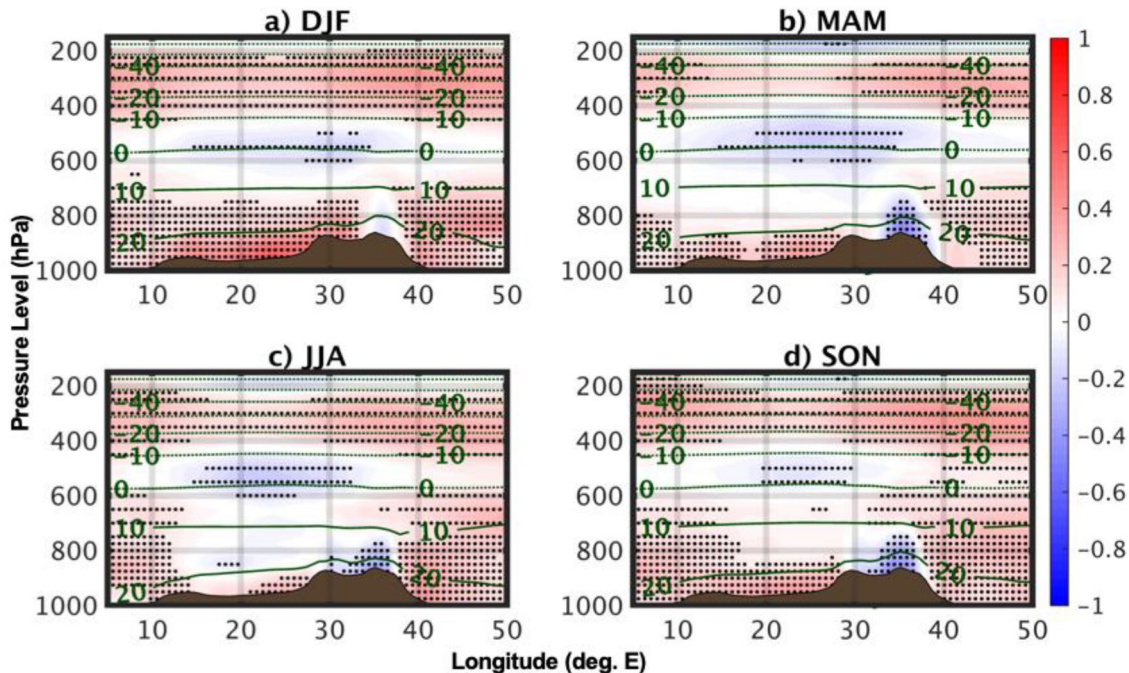


Fig. 9 Seasonal trends in temperature ($10^{-1} \times ^\circ\text{C} \text{year}^{-1}$) at 12:00 UTC from 1983 to 2018. Trends significant at $p < 0.05$ are shown using a black dot. The green lines show the climatological values ($^\circ\text{C}$) from 1983 to 2018

of the θ_e gradient with height indicating a decrease of dry air entrainment, diagnosed using the Π_D . In addition, an

increase in wind shear also appears to contribute to the increase in thunderstorm activity from March–November.

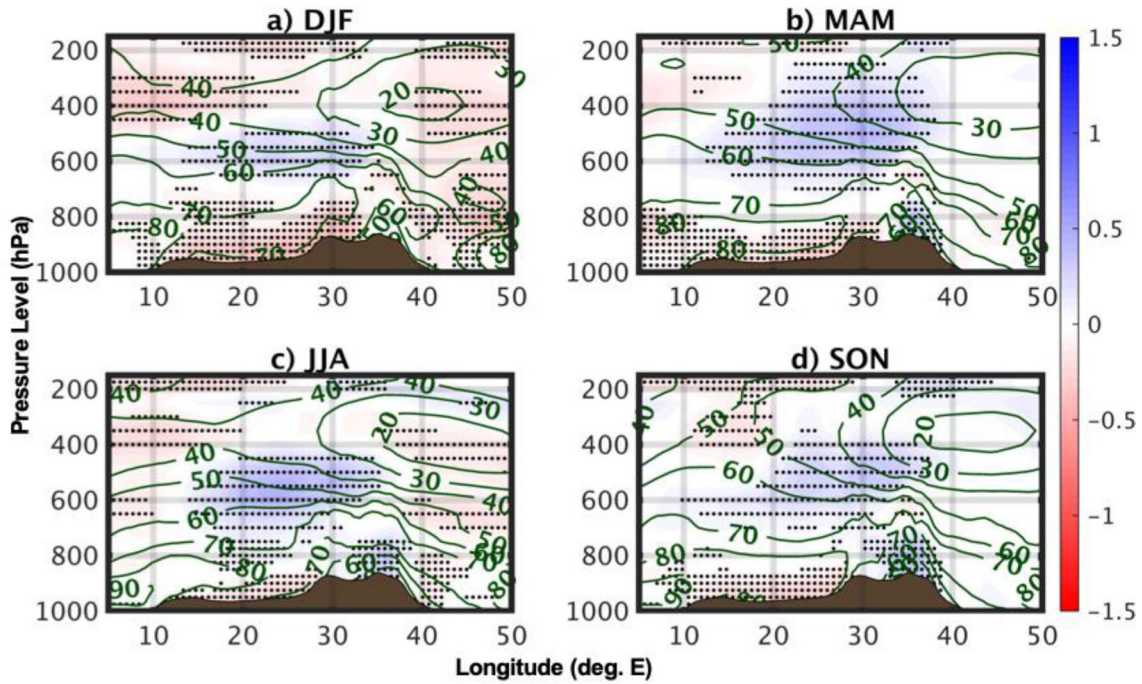


Fig. 10 Seasonal trends in relative humidity ($\% \text{ year}^{-1}$) at 12:00 UTC from 1983 to 2018. Trends significant at $p < 0.05$ are shown using a black dot. The green lines show the climatological values from 1983 to 2018

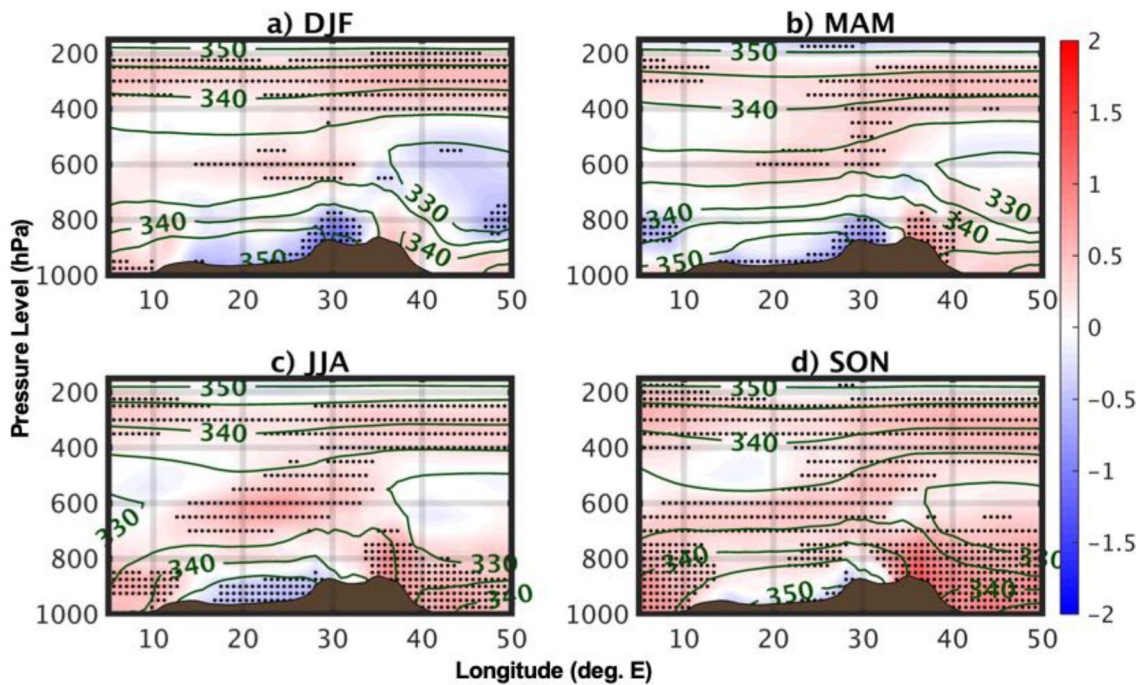


Fig. 11 Seasonal trends in θ_e ($10^{-1} \times \text{K year}^{-1}$) at 12:00 UTC from 1983 to 2018. Trends significant at $p < 0.05$ are shown using a black dot. The green lines show the climatological values (K) from 1983 to 2018

Notwithstanding uncertainties in both satellite and reanalysis datasets (Sect. 2.3), the trends of the GDI and its sub-indices are in good agreement with observations, including in-situ and satellite observations over the study region (e.g., Bush et al. 2020). The temperature profile over the study region (Fig. 9) shows the increase in the occurrence of cold troughs at 500 hPa diagnosed using the MWI, and the increase in the temperature gradient between 700 and 950 hPa diagnosed using the Π_D . In addition, the relative humidity profile (Fig. 10) indicates a drying trend of the lower levels (i.e. Congo Basin) and a moistening of the upper levels. The θ_e profile over the study region is shown in Fig. 11 in order to evaluate the combined trends in temperature and moisture. The decrease of the θ_e gradient with height diagnosed using the Π_D is associated with a decrease of θ_e in the lower troposphere (i.e., the Congo) and an increase of θ_e in the mid/upper troposphere, resulting mostly from a change in moisture (i.e., a decrease in moisture in the lower troposphere and an increase in the mid/upper troposphere) rather than a change in temperature (Soden et al. 2005; Su et al. 2006; Fu 2015; Bush et al. 2020).

The frequent occurrence of cold troughs and cooling at 500 hPa may be a result of an increase in the occurrence of Kelvin waves over the Congo as detected by Raghavendra et al. (2019). An increase in the occurrence of Kelvin waves may lead to an increase in cold ridges at 500 hPa and thus also enhance deep convection over the Congo Basin (Sinclair et al. 2015; Schlueter et al. 2019a, b). On the other hand, a decrease in the θ_e gradient with height may be the combined effect of two processes, a decrease in vegetation greenness and water content associated with droughts over the Congo, and vegetation greening over the East African highlands region (e.g. Hawinkel et al. 2016; Musau et al. 2018; Zhao et al. 2018). Moisture recycling is a crucial process in the tropical rainforests where evapotranspiration contributes substantially to regional precipitation (e.g. Dyer et al. 2017). The large-scale forest browning observed over the Congo, reducing evapotranspiration and decreasing rainfall (Zhou et al. 2014; Hua et al. 2016; Jiang et al. 2019), may reduce the regional moisture supply and thus dry the lower troposphere. The greening over the East African highlands potentially leads to a moistening of the air parcels over the highlands (Musau et al. 2018) before being advected over the Congo Basin by the easterly winds, moistening the air layers aloft the Congo. This could be one reason for the moistening of the mid-troposphere and a decrease in the θ_e gradient with height.

The drying trend in the lower levels (i.e., the Congo Basin) and moistening trend in the mid- and upper troposphere (Fig. 10) may also be the consequence of the increase in deep convection, transporting moisture upwards, drying the lower levels and moistening the mid/upper troposphere. This possibly causes an increase in deep convection, as the

vertical gradient in θ_e is relaxed, which further destabilizes the vertical column and promotes a positive feedback mechanism resulting in taller and more intense thunderstorms. This hypothesis is complemented by previous works such as Soden and Fu (1995) and Zelinka and Hartmann (2009), showing that enhanced tropical convection in a warming climate is responsible for the increased upper-tropospheric relative humidity, with deep convection being the primary source of high clouds and free-tropospheric water vapor through moisture transport to the mid/upper troposphere. The upward transported moisture may then be advected away from the Congo by the poleward flow of the Hadley cell or easterly flow at higher altitudes (Byrne and Schneider 2016). This may possibly lead to less rainfall given the high water recycling ratio over the Congo (Dyer et al. 2017) and could potentially explain the decrease in rainfall detected over the Congo (e.g., Fu 2015; Raghavendra et al. 2018). Further, Figs. 9, 10, 11 suggest that the lifted condensation level (LCL) may have shifted to higher altitudes due to surface drying. Prein and Heymsfield (2020) showed that the melting height level and warm cloud depth has increased over the Congo, possibly affecting cloud microphysics and rainfall characteristics. This supports the hypothesis of a higher LCL, reducing the rainfall reaching the surface, and ultimately causing the drying trend over the Congo Basin as more water or ice particles falling out of a cloud may vaporize before reaching the ground (virga).

In summary, the increase in thunderstorm activity over the Congo Basin is found to be the result of a cooling of the 500 hPa temperature, an increase in the temperature gradient between 700 and 950 hPa, and a decrease of the θ_e gradient with height. The cooling of the 500 hPa temperature may be attributable to an increase in cold troughs, which is hypothesized to be the consequence of an increase in the occurrence of Kelvin waves over the Congo (e.g., Raghavendra et al. 2019). The decrease of the θ_e with height is shown to be the effect of a decrease in moisture in the lower levels and an increase in moisture in the mid and upper levels (Fig. 10). The decrease in moisture in the lower levels is assumed to be a direct effect of the drying trend over the Congo, while the moistening of the mid/upper levels is hypothesized to be a result of a greening and moistening of the East African Highlands (e.g., Musau et al. 2018), from where moist air is being advected over the Congo. Further, the upward transport of moist air during deep convection is hypothesized to additionally destabilize the column and enhance convective processes. The upward transported moisture potentially being advected away by the Hadley cell, and less rainfall reaching the surface due an elevation of the LCL and melting level likely result in a decreasing trend in rainfall and enhanced drying trend over the Congo.

Figure 12 summarizes the key findings of this work, including the observed changes in atmospheric temperature

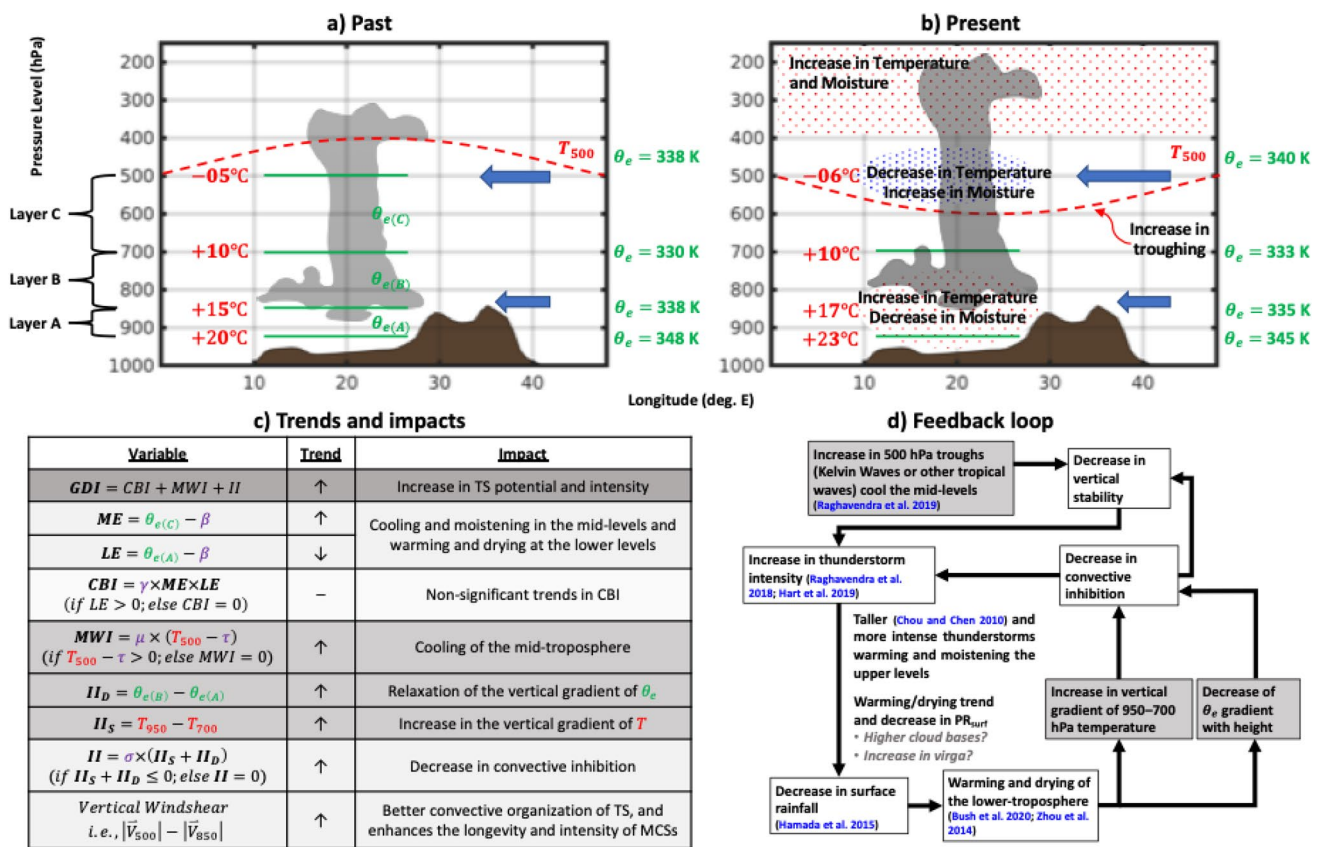


Fig. 12 a, b Schematic of changes in temperature and moisture (diagnosed using the GDI) and wind shear from 1983 to 2018 leading to the observed increase in thunderstorm activity. c Diagnosed trends of the GDI and its sub-indices and their impacts on atmospheric tem-

perature, moisture and stability. d Feedback loop of proposed factors leading to taller and more intense thunderstorms, in turn impacting atmospheric conditions and further enhancing deep convection

and moisture from 1983 to 2018 leading to the detected increase in thunderstorm activity (Fig. 12a, b), trends found in the GDI and its sub-indices including their impacts posed on atmospheric stability (Fig. 12c). It also includes a schematic of the proposed possible physical mechanisms, linking enhanced thunderstorm activity to the observed drying trend found over the Congo (Fig. 12d). In conclusion, thunderstorm activity over the Congo has increased, while rainfall has decreased significantly. The increasing trend in thunderstorm activity may be linked to an increase in the occurrence of cold troughs at 500 hPa, an increase of the temperature gradient between 700 and 950 hPa, and a decrease of the θ_e gradient with height. These mechanisms were also linked together in a positive feedback loop (Fig. 12d) which potentially explain the increase in thunderstorm activity and the decrease in surface rainfall and vegetation over the Congo. The enhanced convective activity likely moistens the mid/upper troposphere, and moisture may be transported away from the Congo Basin by the poleward flow of the Hadley cell and the tropical easterlies. This transport of moisture away from the Congo which is characterized by a large water

recycling ratio could be one possible reason for the observed decrease in rainfall.

From a future climate perspective, significantly more work is necessary to understand rainfall and vegetation characteristics over the Congo Basin. From an observations and historical climate standpoint, there is considerable spread in rainfall estimates amongst datasets (Washington et al. 2013). While studies such as Fotso-Nguemo et al. (2018) have shown the relatively well-known increases in heavy rainfall events in a warmer climate using GCMs for central Africa, the complex orography and overall uncertainties amongst GCMs over the Congo Basin is non-trivial (e.g., Haensler et al. 2013; Washington et al. 2013; Raghavendra et al. 2020a, b). Therefore, the need for high-resolution regional climate models (e.g., Tamoffo et al. 2019) and convection allowing simulations (Stratton et al. 2018) are necessary to further expand our understanding of both the present and future climate for Africa (especially the Congo Basin).

Acknowledgements This work is supported by the National Science Foundation (NSF AGS-1535426 and AGS-1854486). Heather S. Sussman acknowledges the funding support from the Science, Mathematics, and Research for Transformation (SMART) fellowship.

Appendix A: Calculation of θ_e proxies for each layer from specific humidity and temperature, used to calculate the GDI

First, relative humidity (RH) was calculated at every level using specific humidity (q) and temperature (T) from the ERA-I dataset:

$$e^* = 6.112 \exp \left[\frac{17.76T}{T + 243.5} \right] \tag{A1}$$

$$q^* = 0.622 \frac{e^*}{P} \tag{A2}$$

$$RH = \frac{q}{q^*} \times 100 \tag{A3}$$

where e^* is the saturated vapor pressure (hPa) and T is the temperature in °C (Bolton 1980). q^* is the saturation specific humidity and P is the atmospheric pressure (hPa) (Brock and Richardson 2001).

Potential temperature (θ ; K) and mixing ratios (r; kg kg⁻¹) were then calculated for each layer using RH (Gálvez and Davison 2016).

Layer A:

$$\theta_A = \theta_{950} = T_{950} \left(\frac{1000}{950} \right)^{\frac{2}{7}} \tag{A4}$$

$$P_{ws_{950}} = 6.116441 \times 10^{\left[\frac{7.591386 \times T_{950}}{T_{950} + 240.7263} \right]} \tag{A5}$$

$$P_{w_{950}} = P_{ws_{950}} \times \frac{RH_{950}}{100} \tag{A6}$$

$$r_A = \frac{621.9907}{1000} \times \frac{P_{w_{950}}}{950 - P_{w_{950}}} \tag{A7}$$

Layer B:

$$\theta_B = 0.5(\theta_{850} + \theta_{700}) = 0.5 \left[T_{850} \left(\frac{1000}{850} \right)^{\frac{2}{7}} + T_{700} \left(\frac{1000}{700} \right)^{\frac{2}{7}} \right] \tag{A8}$$

$$P_{ws_{850}} = 6.116441 \times 10^{\left[\frac{7.591386 \times T_{850}}{T_{850} + 240.7263} \right]} \tag{A9}$$

$$P_{ws_{700}} = 6.116441 \times 10^{\left[\frac{7.591386 \times T_{700}}{T_{700} + 240.7263} \right]} \tag{A10}$$

$$P_{w_{850}} = P_{ws_{850}} \times \frac{RH_{850}}{100} \tag{A11}$$

$$P_{w_{700}} = P_{ws_{700}} \times \frac{RH_{700}}{100} \tag{A12}$$

$$r_{850} = \frac{621.9907}{1000} \times \frac{P_{w_{850}}}{850 - P_{w_{850}}} \tag{A13}$$

$$r_{700} = \frac{621.9907}{1000} \times \frac{P_{w_{700}}}{700 - P_{w_{700}}} \tag{A14}$$

$$r_B = 0.5(r_{850} + r_{700}) \tag{A15}$$

Layer C:

$$\theta_C = \theta_{500} = T_{500} \left(\frac{1000}{500} \right)^{\frac{2}{7}} \tag{A16}$$

$$P_{ws_{500}} = 6.116441 \times 10^{\left[\frac{7.591386 \times T_{500}}{T_{500} + 240.7263} \right]} \tag{A17}$$

$$P_{w_{500}} = P_{ws_{500}} \times \frac{RH_{500}}{100} \tag{A18}$$

$$r_C = \frac{621.9907}{1000} \times \frac{P_{w_{500}}}{500 - P_{w_{500}}} \tag{A19}$$

where P_{ws} = saturation vapor pressure, P_w = partial pressure of water vapor (Gálvez and Davison 2016).

The θ_e was then calculated, where the following formula from Betts and Dugan (1973), simplified by Bolton (1980) was chosen since the calculation for θ_e is non-trivial:

$$\theta_e = \theta \exp \left(\frac{L_o r}{C_{pd} T_{LCL}} \right) \tag{A20}$$

where $L_o = 2.69 \times 10^6$ J kg⁻¹ is the latent heat of vaporization, $C_{pd} = 1005.7$ J kg⁻¹ K⁻¹ is the specific heat of dry air at constant pressure, and T_{LCL} is the temperature in K at the lifted condensation level LCL.

T_{LCL} was then replaced by the 850 hPa temperature (K) to work around the complex calculation for T_{LCL} , which results in the following calculation of θ_e used to calculate the GDI:

$$\theta_e = \theta \exp \left(\frac{L_o r}{C_{pd} T_{850}} \right) \tag{A21}$$

Gálvez and Davison (2016) tested replacing T_{LCL} by the 850 hPa temperature and only found very small differences on the final GDI values. Therefore, this simplification was used in this study as well.

For each layer, θ_e proxies are then calculated using Eq. A21:

Layer A:

$$\theta_{e(A)} = \theta_A \exp \frac{L_o r_A}{C_{pd} T_{850}} \quad (\text{A22})$$

Layer B:

$$\theta_{e(B)} = \theta_B \exp \frac{L_o r_B}{C_{pd} T_{850}} + \alpha \quad (\text{A23})$$

Layer C:

$$\theta_{e(C)} = \theta_C \exp \frac{L_o r_C}{C_{pd} T_{850}} + \alpha \quad (\text{A24})$$

where $\alpha = -10$ K is an empirical adjustment constant aiming to limit excessive GDI values in regions with plentiful moisture at and above 850 hPa (Gálvez and Davison 2016).

References

- Adler RF, Gu G, Sapiano M, Wang JJ, Huffman GJ (2017) Global precipitation: means, variations and trends during the satellite era (1979–2014). *Surv Geophys* 38:679–699
- Alsordf D et al (2016) Opportunities for hydrologic research in the Congo Basin. *Rev Geophys* 54:378–409
- Anber U, Wang S, Sobel AH (2014) Response of atmospheric convection to vertical wind shear: cloud-system resolving simulations with parameterized large-scale circulation. Part I: specified radiative cooling. *J Atmos Sci* 71:2976–2993
- Betts AK, Dugan FJ (1973) Empirical formula for saturation pseudoadiabats and saturation equivalent potential temperature. *J Appl Meteor* 12:731–732
- Bolton D (1980) The computation of equivalent potential temperature. *Mon Weather Rev* 108:1046–1053
- Brock FV, Richardson SJ (2001) *Meteorological measurement systems*. Oxford University Press, Oxford, p 290
- Buizza R, Houtekamer PL, Toth Z, Pellerin G, Wei M, Zhu Y (2005) A comparison of the ECMWF, MSC, and NCEP global ensemble prediction systems. *Mon Weather Rev* 133:1076–1097
- Bush ER, Jeffery K, Bunnefeld N, Tutin C, Musgrave R, Moussavou G, Mihindou V, Malhi Y, Lehmann D, Edzang Ndong J, Makaga L, Abernethy K (2020) Rare ground data confirm significant warming and drying in western equatorial Africa. *PeerJ* 8:e8732
- Byrne MP, Schneider T (2016) Narrowing of the ITCZ in a warming climate: physical mechanisms. *Geophys Res Lett* 43:11350–11357
- Chou C, Chen C-A (2010) Depth of convection and the weakening of tropical circulation in global warming. *J Climate* 23:3019–3030
- Christian HJ, Blakeslee RJ, Boccippio DJ, Boeck WL, Buechler DE, Driscoll KT, Goodman SJ, Hall JM, Koshak WJ, Mach DM, Stewart MF (2003) Global frequency and distribution of lightning as observed from space by the Optical Transient Detector. *J Geophys Res* 108:4005
- Dai A (2006) Precipitation characteristics in eighteen coupled climate models. *J Climate* 19:4605–4630
- Dee DP, Uppala SM, Simmons AJ et al (2011) The ERA-Interim reanalysis: configuration and performance of the data assimilation system. *Q J R Meteorol Soc* 137:553–597
- Diem J, Ryan S, Hartter J, Palace M (2014) Satellite-based rainfall data reveal a recent drying trend in central equatorial Africa. *Clim Change* 126:263–272
- Dyer ELE, Jones DBA, Nusbaumer J, Li H, Collins O, Vettoretti G, Noone D (2017) Congo Basin precipitation: assessing seasonality, regional interactions, and sources of moisture. *J Geophys Res Atmos* 122:6882–6898
- Fotso-Nguemo TC, Chamani R, Yepdo ZD, Sonkoué D, Matsaguim CN, Vondou DA, Tanessong RS (2018) Projected trends of extreme rainfall events from CMIP5 models over central Africa. *Atmos Sci Lett* 19:1–8
- Fu R (2015) Global warming-accelerated drying in the tropics. *Proc Natl Acad Sci USA* 112:3593–3594
- Gálvez JM, Davison M (2016) The Gálvez-Davison Index for Tropical Convection. https://www.wpc.ncep.noaa.gov/international/gdi/GDI_Manuscript_V20161021.pdf Accessed 24 Apr 2020
- Haensler A, Saeed F, Jacob D (2013) Assessment of projected climate change signals over central Africa based on a multitude of global and regional climate projections. In: Haensler A, Jacob D, Kabat P, Ludwig F (eds) *Climate change scenarios for the congo basin*. Climate Service Centre Report No. 11, Hamburg ((ISSN: 2192-4058))
- Haklander A, van Delden AJ (2003) Thunderstorm predictors and their forecast skill for the Netherlands. *Atmos Res* 67–68:273–299
- Hamada A, Takayabu YN, Liu C, Zipser EJ (2015) Weak linkage between the heaviest rainfall and tallest storms. *Nat Commun* 6:6213
- Hart NCG, Washington R, Maidment RI (2019) Deep convection over Africa: annual cycle, ENSO, and trends in the hotspots. *Bull Am Meteorol Soc* 32:8791–8811
- Hawinkel P, Thiery W, Lhermitte S, Swinnen E, Verbist B, Van Orshoven J, Muys B (2016) Vegetation response to precipitation variability in East Africa controlled by biogeographical factors. *J Geophys Res* 121:2422–2444
- Hua W, Zhou L, Chen H, Nicholson SE, Jiang Y, Raghavendra A (2016) Possible causes of the Central Equatorial African long-term drought. *Environ Res Lett* 11:124002
- Hua W, Zhou L, Nicholson SE, Chen H, Qin M (2019) Assessing reanalysis data for understanding rainfall climatology and variability over Central Equatorial Africa. *Climate Dyn* 53:651–669
- Jackson B, Nicholson SE, Klotter D (2009) Mesoscale convective systems over western equatorial Africa and their relationship to large-scale circulation. *Mon Weather Rev* 137:1272–1294
- James RP, Markowski PM (2010) A numerical investigation of the effects of dry air aloft on deep convection. *Mon Weather Rev* 138:140–161
- Jayakrishnan PR, Babu CA (2014) Assessment of convective activity using stability indices as inferred from radiosonde and MODIS data. *Atmos Climate Sci* 4:122–130
- Jiang Y, Zhou L, Tucker CJ, Raghavendra A, Hua W, Liu Y, Joiner J (2019) Widespread increase of boreal summer dry season length over the Congo rainforest. *Nat Climate Change* 9:617–622
- Knapp KR (2008) Scientific data stewardship of International Satellite Cloud Climatology Project B1 global geostationary observations. *J Appl Remote Sens* 2:023548
- Knapp KR (2012) Intersatellite bias of the high-resolution infrared radiation sounder water vapor channel determined using ISCCP B1 data. *J Appl Remote Sens* 6:063523
- Knapp KR (2016) Gridded Satellite B1 FCDR—Monthly Means. <https://ncics.org/ncics/pdfs/obs4MIPs/GriddedSatelliteB1FC>

- [DR-MonthlyMeans_technical_note_final.pdf](#) Accessed 18 May 2020
- Knapp KR et al (2011) Globally gridded satellite observations for climate studies. *Bull Am Meteorol Soc* 92:893–907
- Lee DE, Biasutti M (2014) Climatology and variability of precipitation in the Twentieth Century Reanalysis. *J Climate* 27:5964–5981
- Marion GR, Trapp RJ (2019) The dynamical coupling of convective updrafts, downdrafts, and cold pools in simulated supercell thunderstorms. *J Geophys Res Atmos* 124:664–683
- Miller PW, Mote TL, Ramseyer CA (2019) An empirical study of the relationship between seasonal precipitation and thermodynamic environment in Puerto Rico. *Bull Am Meteorol Soc* 34:277–288
- Musau J, Patil S, Sheffield J, Marshall M (2018) Vegetation dynamics and responses to climate anomalies in East Africa. *Earth Syst Dyn Discuss* 1–27.
- National Research Council (NRC) (2004) Climate data records from environmental satellites. National Academies Press, Washington, D.C., p 102
- Nicholson SE (2018) The ITCZ and the seasonal cycle over equatorial Africa. *Bull Am Meteorol Soc* 30:337–348
- Perez R, Kivalov S, Schlemmer J, Hemker K Jr, Renné D, Hoff TE (2010) Validation of short and medium term operation solar radiation forecasts in the US. *Sol Energy* 84:2161–2172
- Pokam WM, Djiotang LAT, Mkankam FK (2012) Atmospheric water vapor transport and recycling in Equatorial Central Africa through NCEP/NCAR reanalysis data. *Climate Dyn* 38:1715–1729
- Prein AF, Heymsfield AJ (2020) Increased melting level height impacts surface precipitation phase and intensity. *Nat Climate Change* 10:771–776
- Raghavendra A, Milrad SM (2019) A new metric to diagnose precipitation distribution in transitioning tropical cyclones. *J Oper Meteor* 7:61–77
- Raghavendra A, Zhou L, Jiang Y, Hua W (2018) Increasing extent and intensity of thunderstorms observed over the Congo Basin from 1982 to 2016. *Atmos Res* 213:17–26
- Raghavendra A, Roundy PE, Zhou L (2019) Trends in tropical wave activity from 1980s–2016. *J Climate* 32:1661–1676
- Raghavendra A, Xia G, Zhou L et al. (2020a) Dynamic aspects of orographic enhancement of rainfall over the Congo Basin. *Geophys Res Lett* (in review)
- Raghavendra A, Zhou L, Roundy PE et al (2020b) The MJO's impact on rainfall trends over the Congo rainforest. *Climate Dyn* 54:2683–2695
- Robe FR, Emanuel KA (2001) The effect of vertical wind shear on radiative–convective equilibrium states. *J Atmos Sci* 58:1427–1445
- Schlueter A, Fink AH, Knippertz P, Vogel P (2019a) A systematic comparison of tropical waves over Northern Africa. Part I: influence on rainfall. *J Climate* 32:1501–1523
- Schlueter A, Fink AH, Knippertz P (2019b) A systematic comparison of tropical waves over northern Africa. Part II: dynamics and thermodynamics. *J Climate* 32:2605–2625
- Sinclair Z, Lenouo A, Tchawoua C, Janicot S (2015) Synoptic Kelvin type perturbation waves over Congo basin over the period 1979–2010. *J Atmos Sol Terr Phys* 130–131:43–46
- Soden BJ, Fu R (1995) A satellite analysis of deep convection, upper tropospheric humidity, and the greenhouse effect. *J Climate* 8:2333–2351
- Soden BJ, Jackson DL, Ramaswamy V, Schwarzkopf D, Huang X (2005) The radiative signature upper tropospheric moistening. *Science* 310:841–844
- Stratton RA et al (2018) A Pan-African Convection-Permitting Regional Climate Simulation with the Met Office Unified Model: CP4-Africa. *J Climate* 31:3485–3508
- Su H, Read WG, Jiang JH, Waters JW, Wu DL, Fetzer EJ (2006) Enhanced positive water vapor feedback associated with tropical deep convection: New evidence from Aura MLS. *Geophys Res Lett* 33:L05709
- Tamoffo AT, Moufouma-Okia W, Dosio A et al (2019) Process-oriented assessment of RCA4 regional climate model projections over the Congo Basin under 1.5°C and 2°C global warming levels: influence of regional moisture fluxes. *Climate Dyn* 53:1911–1935
- Taylor CM et al (2018) Earlier seasonal onset of intense Mesoscale Convective Systems in the Congo Basin since 1999. *Geophys Res Lett* 45:13458–13467
- Uma KN, Das SK (2019) Do the stability indices indicate the formation of deep convection? *Meteorol Atmos Phys* 131:1–10
- Washington R, James R, Pearce H, Pokam WM, Moufouma-Okia W (2013) Congo Basin rainfall climatology: can we believe the climate models? *Philos Trans R Soc B* 368:20120296
- Wedam GB, McMurdie LA, Mass CF (2009) Comparisons of model forecast skill over the east and west coasts of the United States. *Weather Forecasting* 24:843–854
- Yang GY, Slingo J (2001) The diurnal cycle in the Tropics. *Mon Weather Rev* 129:784–801
- Zelinka MD, Hartmann DL (2009) Response of humidity and clouds to tropical deep convection. *J Climate* 22:2389–2404
- Zhao L, Dai A, Dong B (2018) Changes in global vegetation activity and its driving factors during 1982–2013. *Agric For Meteorol* 249:198–209
- Zhou L et al (2014) Widespread decline of Congo rainforest greenness in the past decade. *Nature* 509:86–90
- Zipser E, Liu C, Cecil D, Nesbitt S, Yorty D (2006) Where are the most intense thunderstorms on Earth? *Bull Am Meteorol Soc* 87:1057–1107

Publisher's Note Springer Nature remains neutral with regard to jurisdictional claims in published maps and institutional affiliations.